Supplementary Information

Microporous Membrane with Ionized Sub-nanochannels Enabling Highly Selective Monovalent and Divalent Anion Separation

Mei-Ling Liu[1,2], Yu Chen[1], Chuan Hu[3], Chun-Xu Zhang[1], Zheng-Jun Fu[1], Zhijun Xu[1], Young Moo Lee*[3], Shi-Peng Sun*[1,2,4]

[1]State Key Laboratories of Materials-Oriented Chemical Engineering, National Engineering Research Center for Special Separation Membranes, College of Chemical Engineering, Nanjing Tech University, Nanjing 211816 China
[2]NJTECH University Suzhou Future Membrane Technology Innovation Center, Suzhou 215100, China
[3]Department of Energy Engineering, College of Engineering, Hanyang University, Seoul 04763, Republic of Korea
[4]Suzhou Laboratory, Suzhou 215100, China

These authors contributed equally: Mei-Ling Liu, Yu Chen
E-mail: ymlee@hanyang.ac.kr; ssp@ njtech.edu.cn

Supplementary Methods

Materials

Dimethoxymethane (DMM, 98%, Macklin) and o-benzidine (DMB, 98%, Aladdin) were employed as the reactants, and trifluoroacetic acid (TFA, 99.9%, Macklin) was used as the catalyst for the synthesis of TB polymers. N-Methyl-pyrrolidone (NMP, 99.0%, Macklin) was employed as the solvent for membrane preparation. To enhance the mechanical strength of the membrane, dioctyl phthalate (DOP, 99.0%, Aladdin) was incorporated as an additive. Sodium chloride (NaCl, 99.5%, Aladdin), sodium carbonate (Na_2CO_3, 99.5%, Macklin), and sodium sulfate (Na_2SO_4, 99%, Aladdin) were acquired for testing ion separation performance. Potassium carbonate (K_2CO_3, 99.0%, Shanghai Lingfeng Chemical Reagent Co.) and iodomethane (CH_3I, Shanghai Bailingway Chemical Technology Co.) were procured to facilitate the quaternization process of TB polymers. Polyetheretherketone (PEEK, Shanghai Jizhi Biochemical Technology Co.) and sulfuric acid (H_2SO_4, 95.0%-98.0%, Sinopharm Group Chemical Reagent Co.) were utilized to obtain sulfonated PEEK for the preparation of cation exchange membranes.

Characterization

Fourier Transform Infrared (FT-IR, Thermo Nicolet 8700, USA) spectroscopy was used to observe changes in characteristic peaks ranging from 4000-500 cm^{-1}. A Nuclear Magnetic Resonance instrument (^1H NMR, VNMRS 600 MHz, Varian, CA, USA) was utilized to confirm the chemical structure of the polymer. The sample needed to be dissolved in DMSO-d6, and TFA was added to eliminate the water effects. Gel Permeation Chromatography (GPC, Shimadzu LC-20A, Japan) was used to test the molecular weight of polymers by completely dissolving TB and QA-TB polymers in the N-Methylpyrrolidone. X-ray photoelectron spectroscopy (XPS, Thermo Fisher Scientific, USA) was used to observe the quaternization degree of membranes. The thermo-mechanical characteristics of the membranes including the glass transition temperature (T_g) and storage modulus were evaluated with a dynamic thermomechanical analyzer (DMA, Q800 TA Instrument, DE, USA). Each sample (9 × 20 mm) was tested under a preload force of 0.01 N and 125% of the force track. The heating process occurred at a rate of 4°C per minute, spanning a temperature range of 50 to 700°C under a nitrogen (N_2) environment. The surface charge properties of membranes were assessed by Solid Surface Zeta Potentiometry (ZETA, Anton Paar SurPASS 3, Austria). Samples were affixed within the analyzer, and a 1 mM KCl solution was circulated through them. The pH was increased incrementally to 10 with a 0.1 mol L^{-1} NaOH solution and subsequently stepwise lowered via automated titration using 0.1 mol L^{-1} HCl. The variation in ZETA potential was recorded at pH 2.5. The morphology of membranes was observed by a field emission scanning electron microscope (FESEM, Hitachi S4800). Before observation, the membranes were freeze-dried to remove residual water and then coated with a thin layer of gold nanoparticles. Atomic Force Microscopy (AFM, Veeco, NY, USA) provided a comprehensive insight into the microphase separation of the membranes. A scanning area of 5 μm × 5 μm was

surveyed for each sample at a frequency of 1 Hz in tapping mode. Peak and valley in AFM images represent the roughness of the surface of the membranes as the principle of AFM is using tapping mode of the needles. When casting ionic polymers on the glass plate, film surface is exposed to the air, whereas the bottom side is toward the glass plate. Air is hydrophobic and the glass plate is regarded as hydrophilic. After casting, hydrophobic chains migrate toward the air side of the surface, resulting in hydrophobic bright regions in the valley part. Additionally, as the needle in AFM taps the surface of the membrane, hard and hydrophobic groups are more rigid than the flexible soft and hydrophilic regions, therefore peak regions appear in dark regions and vice versa. Therefore, the bright regions represent the hydrophobic segments of the polymer backbone, whereas the dark regions correspond to the hydrophilic portions. The mechanical strength of the membranes was scrutinized using a universal testing machine (Xinsansi CMT-6203, Shenzhen) at room temperature. Each sample was cut into strips measuring 1 cm × 5 cm with a thickness spanning 150-200 μm and subjected to stretching at a rate of 10 mm per minute. The average data from three distinct tests were utilized. The membrane porosity was observed by N_2 and CO_2 adsorption/desorption through an automatic rapid specific surface and porosity analyzer (Micromeritics ASAP2460, USA). Meanwhile, the microporous sizes of the membranes were measured and analyzed by PALS (DPLS3000) based on the annihilation radiation of the positions in condensed matter to obtain the internal microstructure and the pore size and free volume of the membranes.

Synthesis of TB copolymers

The TB polymer was synthesized through a condensation reaction that engaged DMM and DMB, with TFA serving as both solvent and catalyst. DMB (7.83 g, 0.037 mol) and DMM (14.09 g, 0.185 mol) were mixed in a round-bottom flask. Subsequently, TFA (75 mL, 0.980 mol) was slowly added drop by drop for about 1 hour in an ice bath. Subsequently, the solution was stirred for 96 hours at room temperature to ensure complete reactivity. The resulting polymers were precipitated in deionized water. The residual acidic components of the reaction were rinsed with deionized water to a neutral pH. After that, the solid was filtered and oven dried at 60°C for the following synthesis (98.45% yield).

Synthesis of quaternized TB polymers (QA-TB)

TB polymers (5 g, 0.016 mol) and K_2CO_3 (8 g, 0.058 mol) were mixed in NMP (100 mL, 1.039 mol). In the dark, CH_3I (8 mL, 0.129 mol) was introduced drop by drop. The resultant solution was stirred at room temperature for 24 hours to facilitate quaternization of TB polymers. Subsequently, the mixture was poured into deionized water to precipitate the polymer, and the residual K_2CO_3 was washed with deionized water until no white particles remained. The desiccated polymer was hermetically sealed and placed within a desiccator for storage.

Synthesis of sulfonated polyetheretherketone (SPEEK)

PEEK (9 g, 0.027 mol) was dissolved in H_2SO_4 (150 mL, 2.814 mol) and subjected to stirring at room temperature for 48 hours. The resulting reaction product was

precipitated in chilled deionized water, washed until reaching a neutral pH, and filtered before being dried at 50°C[1].

Model Construction

The system energy calculations were carried out by using the Vienna ab initio simulation package (VASP) code[2]. The generalized gradient approximation (GGA) as well as the Perdew-Burke-Ernzerhof (PBE) functional was used to describe the exchange correlation interactions and the projector augmented wave (PAW) method was used to describe the ionic potential[3, 4]. The plane-wave kinetic energy cutoff was set as 500 eV. A 4×4×4 Monkhorst-Pack k-point mesh was used for the Brillouin zone sampling in all the calculations[5]. For structure relaxation and electronic calculations, the energy convergence criteria for electronic relaxation was set as 1×10^{-5} eV, and the ionic relaxation was performed until all forces were smaller than 0.01 eV/Å. The electron number of the system was controlled by the NELECT parameter, and the adsorption energies (ΔE_{ads}) were calculated by using the following equation (1)[6]:

$$\Delta E_{ads}=E_{total}-E_{sub}-E_{mol} \quad (1)$$

where E_{total} is the total energy of ions adsorbed on substrates, E_{sub} is the total energy of substrates, and E_{mol} is the energy of adsorbed ions. The energy required for ion to desorb from the QA-TB surface could be calculated by the following formula (2)[7]:

$$\Delta E_{des}=E_{s}-E_{u} \quad (2)$$

where ΔE_{des} is the desorption energy, E_s is the total energy of ions on QA-TB, and E_u is the total energy of ions at an infinite distance.

Water Uptake (WU) and Swelling Ratio (SR)

AEM samples were dried overnight in an oven at 80°C to remove absorbed water. Then, their length (L_{dry}) and weight (W_{dry}) were measured, and the samples were immersed in deionized water for 24 hours. The residual water on the membrane surface was removed, and the wet length (L_{wet}) and weight (W_{wet}) were recorded. The *WU* and *SR* could be determined using the following equations (3) and (4):

$$WU(\%)=\frac{W_{wet}-W_{dry}}{W_{dry}}\times 100\% \quad (3)$$

$$SR(\%)=\frac{L_{wet}-L_{dry}}{L_{dry}}\times 100\% \quad (4)$$

Intrinsic viscosity

The intrinsic viscosity ([ŋ]) of the polymers was measured using a Schott Viscometry System (AVS 370, Germany) in a DMSO solution at 25℃. The Schott Viscosystem (AVS 370, Germany) was composed of an Ubbelohde viscometer (SI Analytics, Type 530 13: Capillary No. Ic, K = 0.03) and automatic piston burette (TITRONIC universal). First, a target sample was dissolved in DMSO to form a 3 mg mL^{-1} polymer solution. Then, the solution was automatically diluted into five concentrations in order (3.0, 2.5, 2.0, 1.5, and 1.0 mg mL^{-1}), and five efflux times were recorded. The intrinsic viscosities

([ɳ]) of polymers could be calculated from the following equation (5):

$$\eta=\frac{ln\left(\frac{t_s}{t_b}\right)}{c} \tag{5}$$

where t_s (s) and t_b (s) are the efflux time of DMSO and the polymer solution, respectively, c (g dL^{-1}) is the concentration.

Ion Exchange Capacity (IEC)

The dried QA-TB membrane was circulated in a Na_2SO_4 salt solution for 24 hours with an electric field. Subsequently, the possible residual salt solution on the membrane surface was rinsed several times with pure water, wiped dry, and immersed in a NaCl salt solution for 24 hours. The Ion Exchange Capacity (IEC) of the membrane was calculated according to the following equation (6):

$$IEC=\frac{(c_{1Cl^-}-c_{2Cl^-})\cdot V}{M_{dry}} \tag{6}$$

where c_{1Cl^-} and c_{2Cl^-} are the respective concentrations of Cl^- before and after immersing the membrane, V represents the volume of NaCl solution, and M_{dry} is the quantity of the membrane sample after initial drying.

Ion conductivity

The ion conductivity of the membranes was recorded using an electrochemical workstation (Chen Hua CHI 660E, Shanghai). The samples were evaluated from 30 to 80°C, and the ion conductivity (σ) was calculated by the following equation (7):

$$\sigma=\frac{d}{S\cdot R} \tag{7}$$

where d is the thickness of the membrane (cm), S is the contact area (cm^2), and R is the membrane resistance (Ω).

Current efficiency (η) and energy consumption ratio (W)

The current efficiency and energy consumption ratio could be calculated by the following equations (8) and (9):

$$\eta(\%)=\frac{ZFc_cV_c}{\int_0^t Idt}\times 100\% \tag{8}$$

$$W\left(W\cdot h\cdot mol^{-1}\right)=\frac{U\int_0^t Idt}{N} \tag{9}$$

where Z is the ionic valence, and F is the Faraday constant with a value of 96,485 C mol^{-1}, c_c (mol L^{-1}) is the concentration of the target ion in the concentration chamber, V_c is the volume of the solution in the concentration chamber, I is the current in amperes (A), U is the voltage in volts (V), and N is the mole number of target ions in the concentration chamber.

Supplementary figures

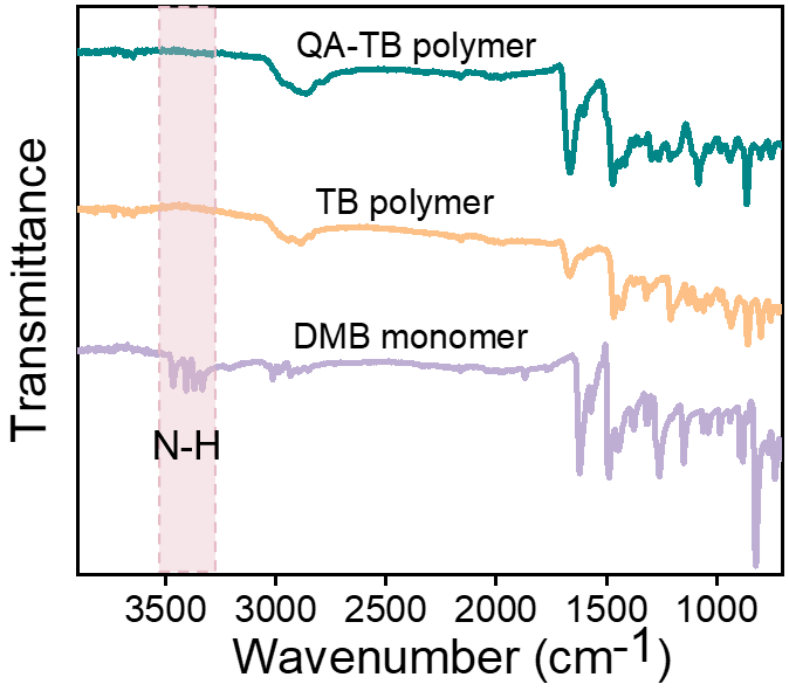

Supplementary Fig. 1 Fourier transform infrared (FT-IR) spectra of the DMB monomer, TB, and QA-TB polymers.

Note: FT-IR indicated absence of the N-H absorption peak of DMB within the range of 3400-3500 cm^{-1} after the formation of the TB group.

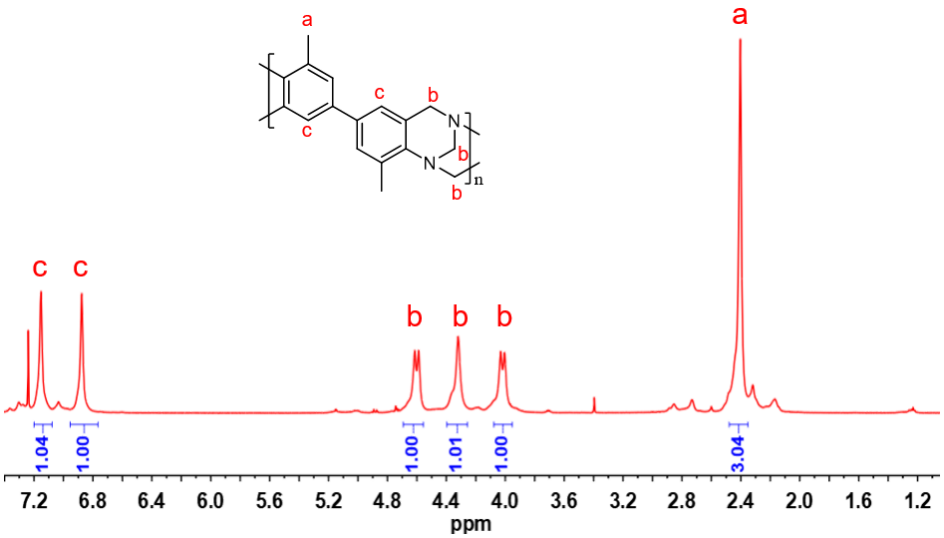

Supplementary Fig. 2 ^{1}H Nuclear magnetic resonance (^{1}H NMR) hydrogen spectra of the TB polymer (600 MHz, DMSO-d6 was used as solvent).

Note: ^{1}H NMR revealed that H_a near 2.4 ppm is the methyl group, H_b in the region of 4.0-4.7 ppm is the methylene group that constitutes the V structure of the TB unit, and H_c between 6.8 and 7.2 ppm is the C-H of the benzene ring. These findings are consistent with the FT-IR results and confirm the successful synthesis of the TB polymer from DMB and DMM.

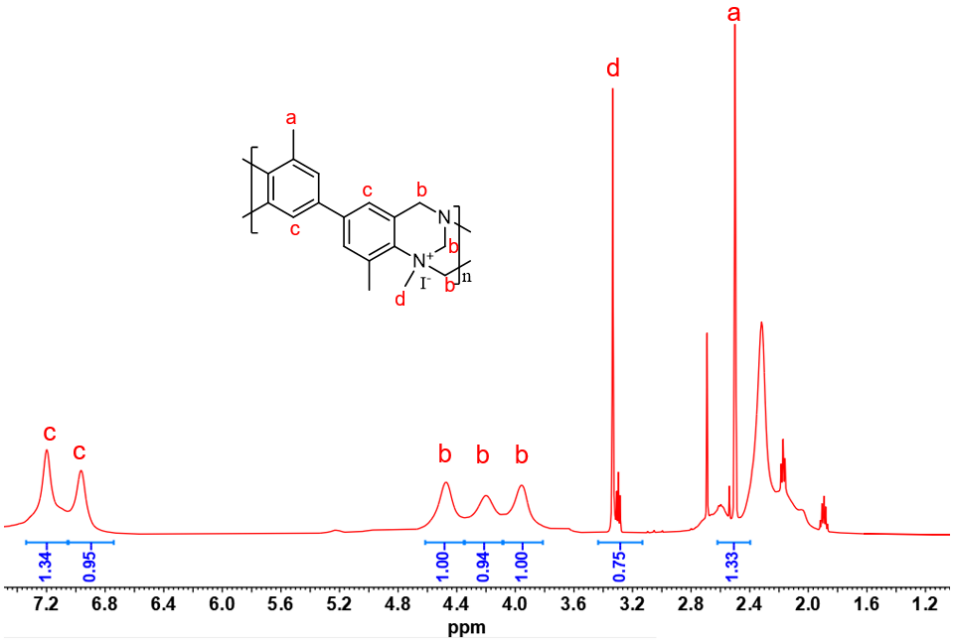

Supplementary Fig. 3 ^{1}H Nuclear magnetic resonance (^{1}H NMR) hydrogen spectra of the QA-TB polymer (600 MHz, DMSO-d6 was used as solvent).

Note: The new peak near 3.3 ppm is attributed to an additional methyl group attached to N, a consequence of the quaternization process.

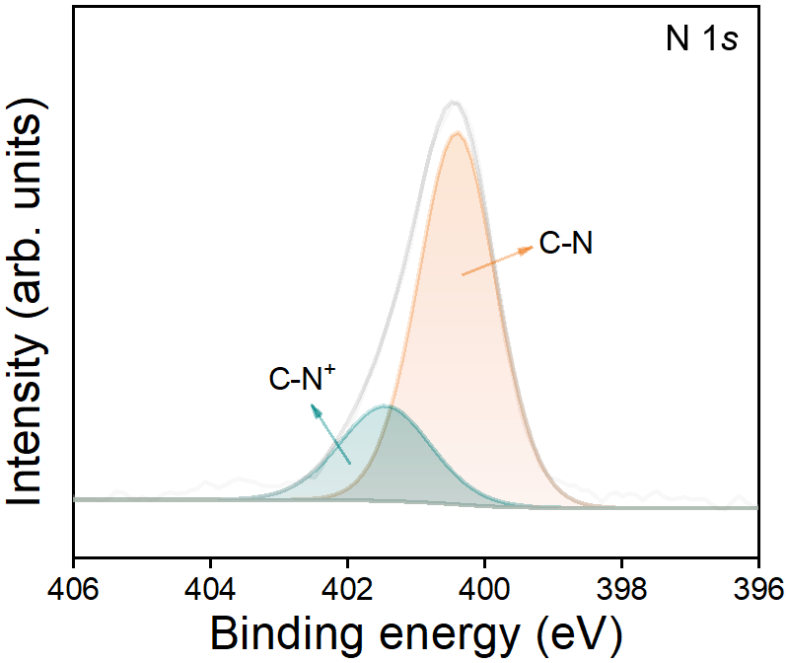

Supplementary Fig. 4 X-ray photoelectron spectroscopy (XPS) spectra of QA-TB membrane.

Note: The appearance of the C-N^+ peak confirms successful quaternization of the TB membrane. Comparing the peak areas of C-N^+ and C-N revealed that the degree of quaternization of TB is approximately 30%. This degree of quaternization avoids excessive hydrophilic quaternary ammonium groups that increase membrane brittleness and reduce mechanical strength, while ensuring sufficient adsorption sites in the ionized sub-nanochannels to promote ion migration.

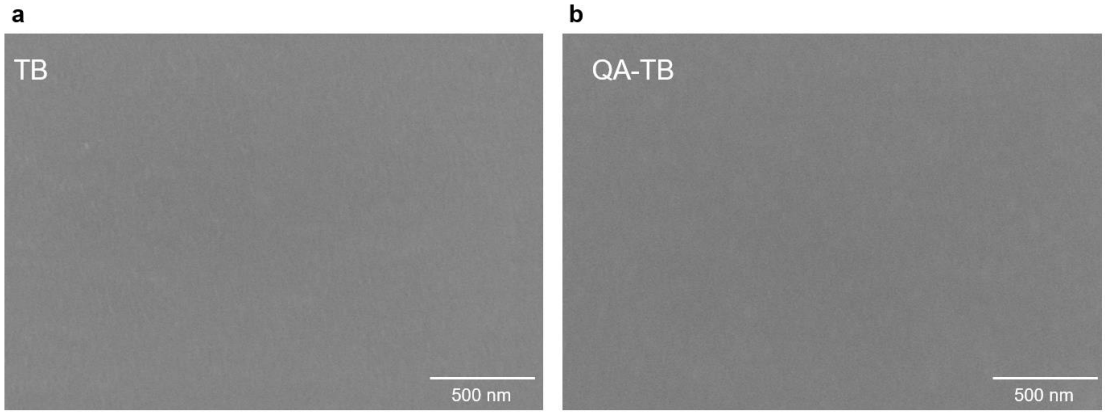

Supplementary Fig. 5 Surface morphologies of (a) TB and (b) QA-TB membranes.

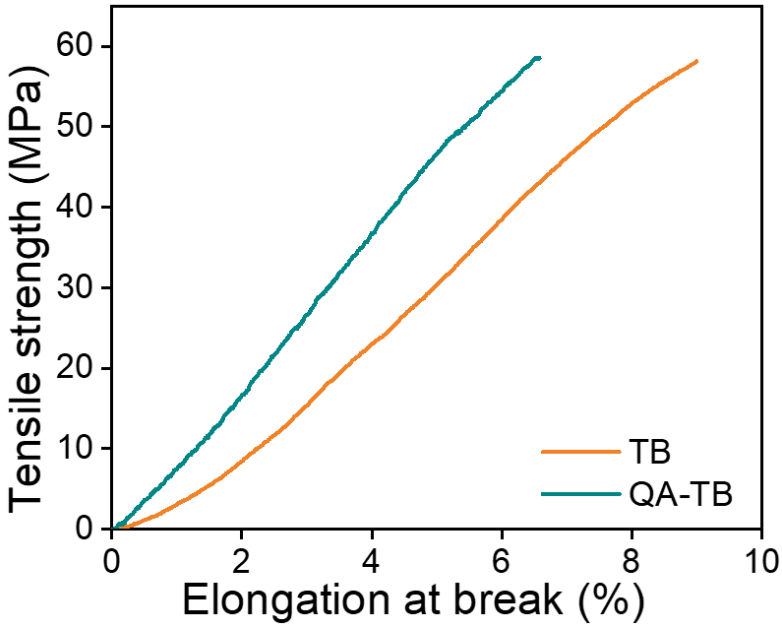

Supplementary Fig. 6 Tensile stress-strain of TB and QA-TB membranes.

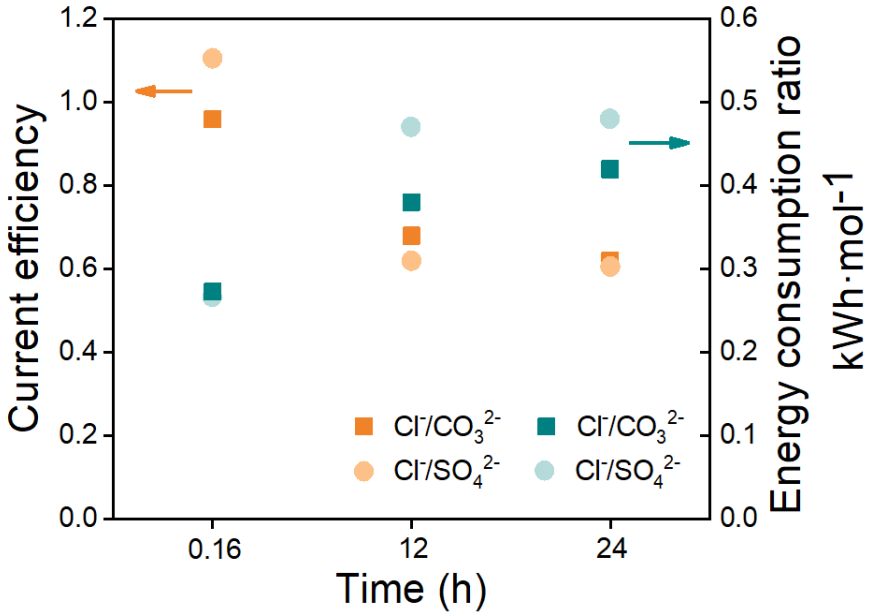

Supplementary Fig. 7 Energy consumption of the QA-TB membrane in different systems.

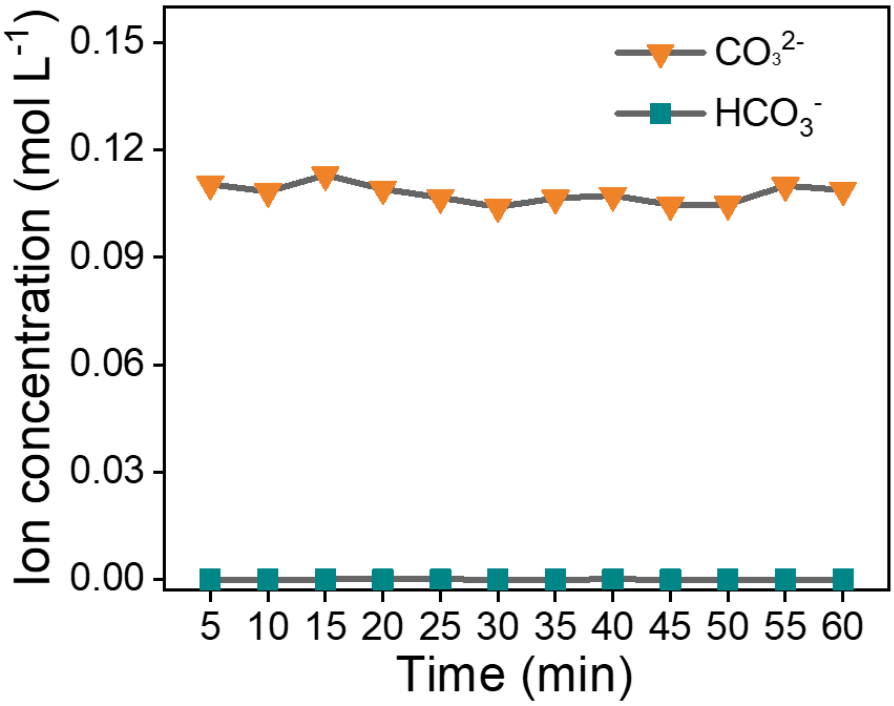

Supplementary Fig. 8 Ion concentrations of CO_3^{2-} and HCO_3^- in the dilution chamber.

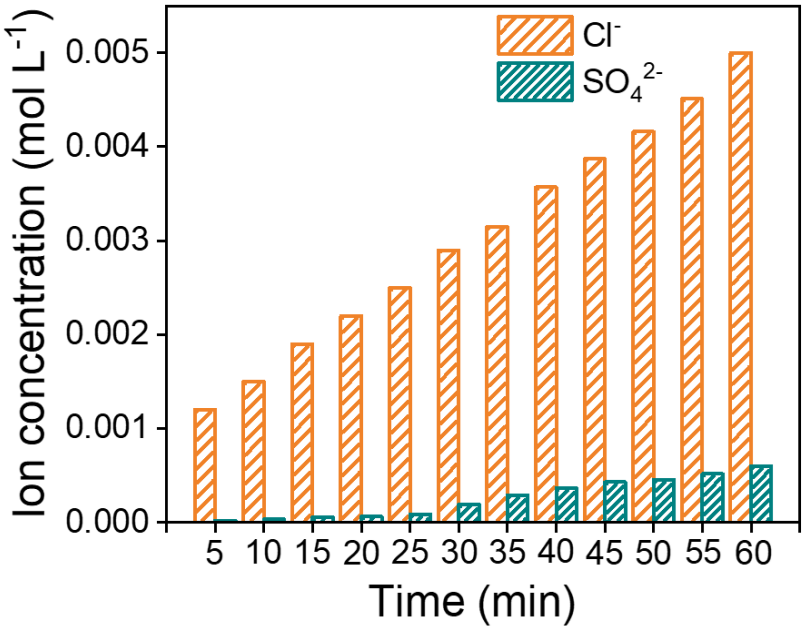

Supplementary Fig. 9 Separation performance of Cl^-/SO_4^{2-} over 1 hour.

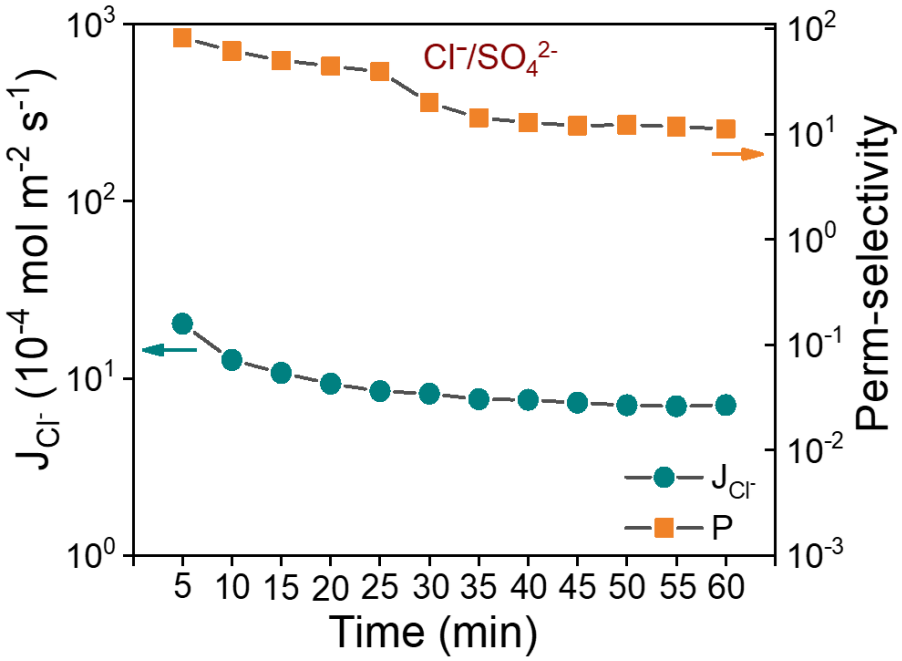

Supplementary Fig. 10 Cl^- flux and selectivity in the Cl^-/SO_4^{2-} separation system.

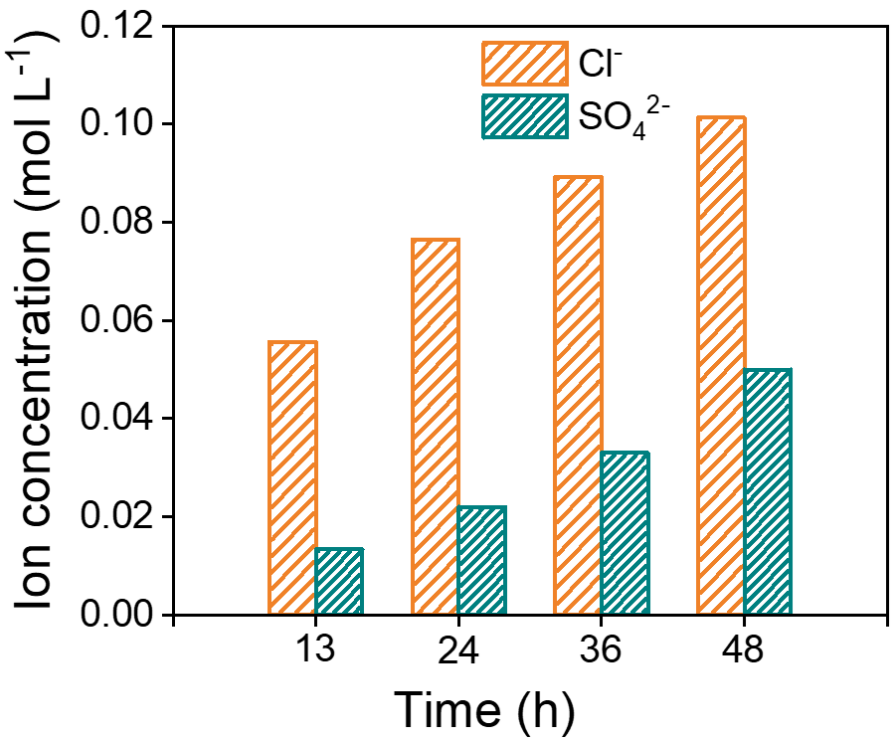

Supplementary Fig.11 Ion concentration in the concentration chamber.

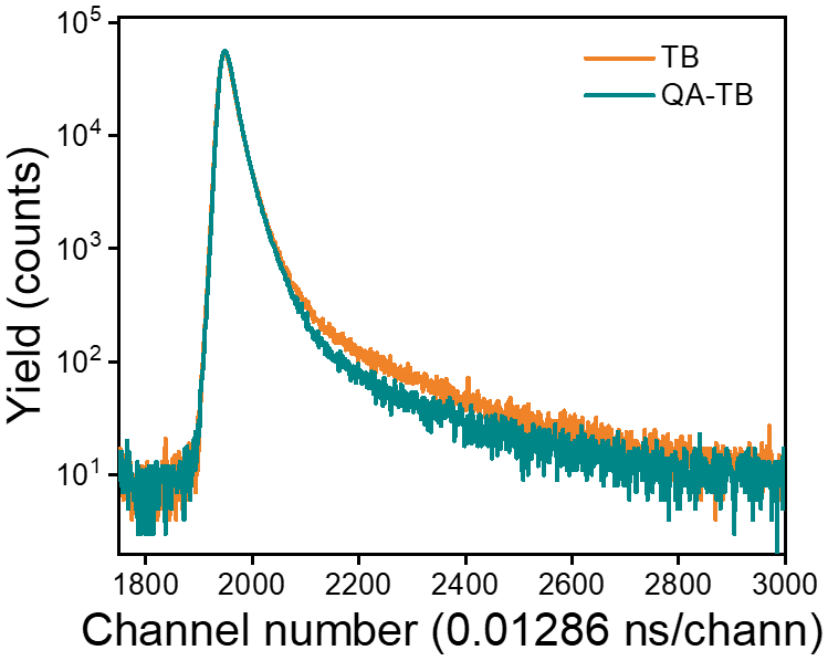

Supplementary Fig. 12 Normalized positron annihilation lifetime spectra (PALS) of the TB and QA-TB membranes.

Note: PALS reflects the membrane microstructure based on the time for positrons to be generated from a radioactive source and annihilate electrons upon entering the material. The intrinsic microporosity size, distribution, and free volume of the membranes were determined by analyzing the peak-normalized positron lifetime spectra using the CONTIN and PATFIT programs.

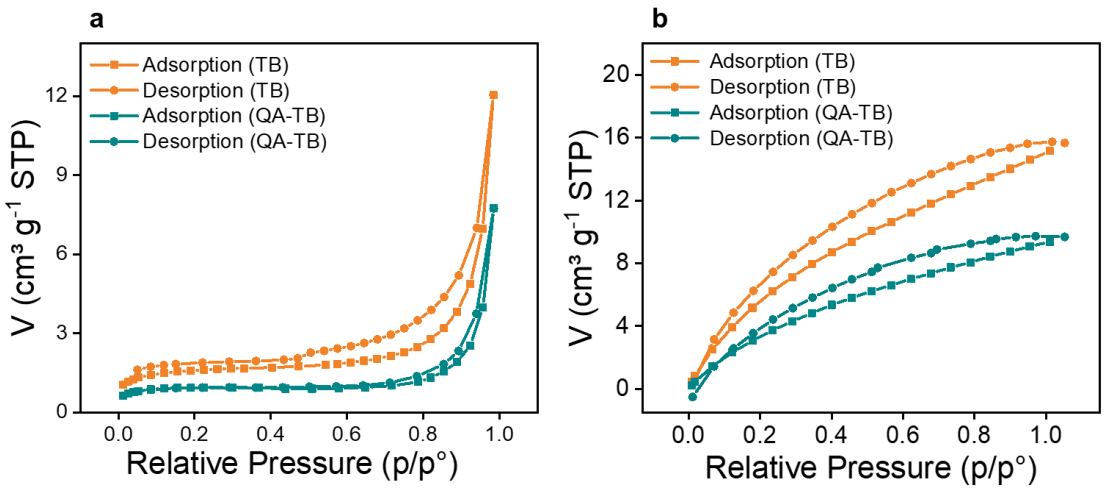

Supplementary Fig. 13 (a) N_2 and (b) CO_2 adsorption/desorption curve of the TB/QA-TB membrane.

Note: CO_2 is primarily used to probe microporous pores smaller than 2 nm, while N_2 is mainly used to test mesopores or macropores. Due to its smaller size and faster diffusion rate compared to N_2, CO_2 more easily reaches saturated adsorption. PALS results indicate that the TB and QA-TB in this work have pore sizes less than 1 nm, classifying them as microporous structures. Consequently, N_2 adsorption is lower than that of CO_2. Additionally, compared to the TB membrane, the reduced adsorption on the QA-TB membrane is due to the quaternary ammonium modification, which strengthens ion/polar chain interactions, resulting in narrower membrane pores.

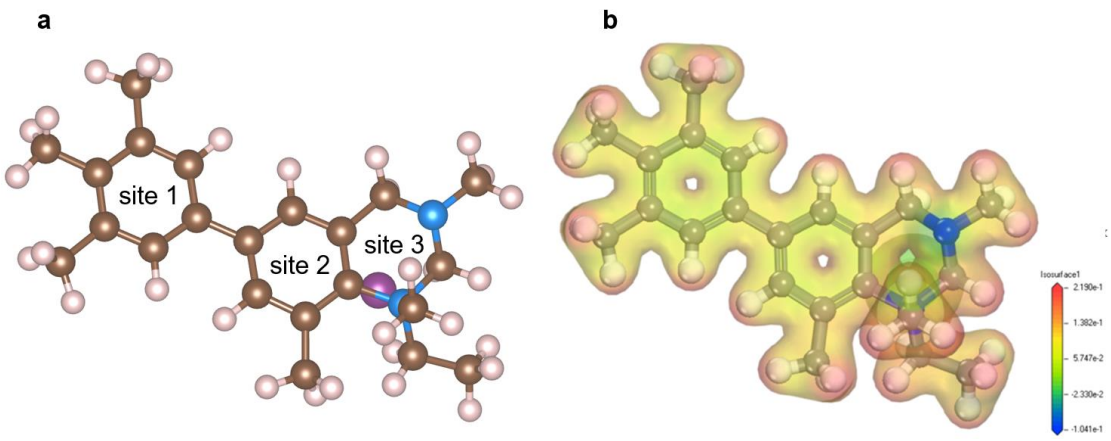

Supplementary Fig. 14 a Structural optimization and **b** electrostatic potential map for the QA-TB model.

Note: Structural optimization of QA-TB shows three distinct active sites conducive to ion adsorption. Site 1 and site 2 are located at the center of the benzene ring, and site 3 is the N-N bridge position. The electrostatic potential diagram of QA-TB was then calculated to observe the charge distribution. The blue atom represents nitrogen in the TB group, and the purple atom signifies iodine introduced during quaternization. The electrostatic potential map of QA-TB reveals that the positive charge of the QA group enhances the electrophilic nature of the system. Meanwhile, anion neutralization (site 3) within the system attenuates the interaction between QA-TB and anions, facilitating anion desorption.

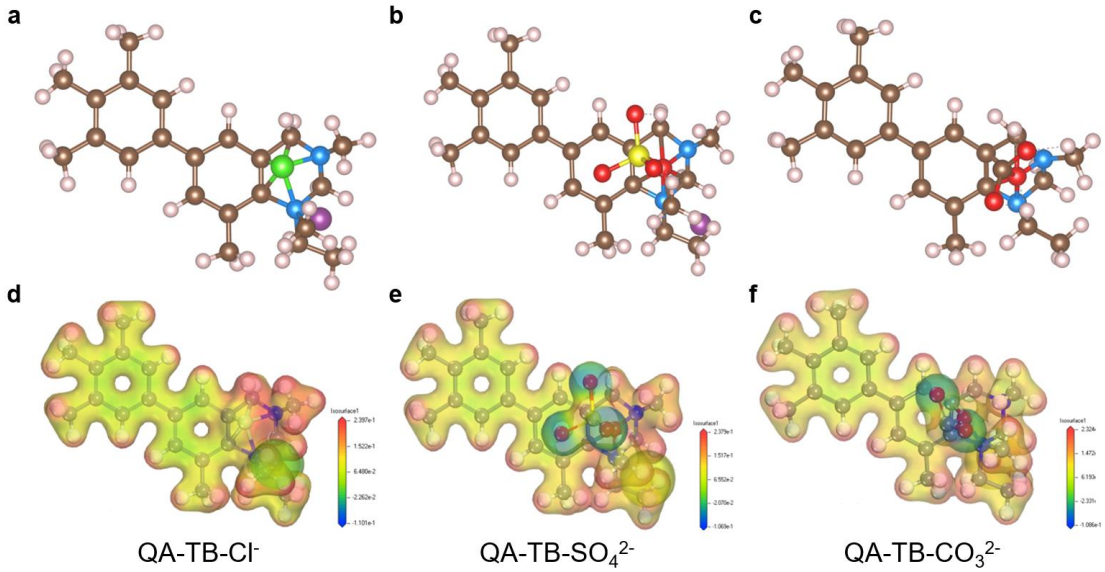

Supplementary Fig. 15 Optimal adsorption configurations and electrostatic potential maps of anions on the QA-TB surface. **a, d** QA-TB-Cl^-; **b, e** QA-TB-SO_4^{2-}; **c, f** QA-TB-CO_3^{2-}.

Note: The adsorption properties of $Cl^-/SO_4^{2-}/CO_3^{2-}$ ions at different sites on the QA-TB were calculated by constructing optimal adsorption configurations (**Supplementary Table 6**). All three ions preferentially adsorb at site 3 due to the electrostatic interactions with the quaternary ammonium groups.

Supplementary Table 1 Comparison of water uptake and swelling ratios of TB and QA-TB membranes with other membranes in the literature.

Type of membrane	WU (%)	SR (%)	Reference
QAPIB	23.7±1.0	4.2±0.2	8
QC-AEM-1	16.2	5.8	9
B0	16±2.5	5.7	10
PVC-Im-4C	16.07	3.62	11
IM-PAES-sIM	15.2±1.0	7.5±0.5	12
Im-AP-2	14.54±1.5	2.67±0.9	13
QAPCE-10C	6.3±0.56	3.8±0.26	14
c-PPO-Im-65	5.6	2.4	15
TB	4.05±0.35	0.89±0.13	This work
QA-TB	1.75±0.30	1.01±0.02	This work

Supplementary Table 2 Properties of the prepared TB and QA-TB membranes.

Type of membrane	TB	QA-TB
Water Uptake (%)	4.05±0.35	1.75±0.30
Swelling Ratio (%)	0.89±0.13	1.01±0.02
Tensile strength (MPa)	58.15	58.53
Storage modulus (MPa)	1267	1629
Glass transition temperature (°C)	410	338
Zeta potential (mV)	-14	-31
Conductivity (mS cm^{-1})	7.63	12.23
J_{Cl^-} ($\times 10^{-4}$ mol m^{-2} s^{-1})	4.07	16.13
M_W (g mol^{-1})	74826	76108
Intrinsic viscosity (dL g^{-1})	0.81	1.06

Note: The basic properties of the polymer membranes are summarized. Both membranes show low swelling in addition to remarkable thermal and mechanical stabilities.

Supplementary Table 3 Comparison of monovalent and divalent anion separation performance of QA-TB membrane with previously reported membranes.

Type of membranes	Separation system	Monovalent anion flux ($\times 10^{-4}$ mol m^{-2} s^{-1})	Permeation selectivity	Reference
PAES-UIO-66-Pyr	Cl^-/SO_4^{2-}	1.4	54.26	16
QDPAB-C7	Cl^-/SO_4^{2-}	10.56	15.7	17
HPABP-CC3(15)	Cl^-/SO_4^{2-}	6.22	12.67	18
QP-P3-1	Cl^-/SO_4^{2-}	4.2	6.7	19
QP-P6-1	Cl^-/SO_4^{2-}	4.3	9.3	19
QP-P11-1	Cl^-/SO_4^{2-}	3	13.07	19
PPO-0.100-ImPS	Cl^-/SO_4^{2-}	16.2	16.12	20
sCOF/aAEM3	Cl^-/SO_4^{2-}	3.35	18.92	21
Blend-15 AIEM	Cl^-/SO_4^{2-}	3.25	21.8	22
Blend-10 AIEM	Cl^-/SO_4^{2-}	2.4	14	22
Blend-0 AIEM	Cl^-/SO_4^{2-}	3.25	11.3	22
PAES-im-2.5c AIEM	Cl^-/SO_4^{2-}	3.7	12.5	23
Neosepta ACS	Cl^-/SO_4^{2-}	2.1	5.27	23
MQ18	Cl^-/SO_4^{2-}	14.5	16.7	24
AF1-HNN5-50	Cl^-/SO_4^{2-}	29.2	62.2	25
PQC76/DSA-0.5	Cl^-/SO_4^{2-}	5	10.38	26
PAES-UIO-66-Py	NO_3^-/SO_4^{2-}	2.19	55.9	16
QA-TB	Cl^-/SO_4^{2-}	20.37	82	This work
QA-TB	Cl^-/CO_3^{2-}	16.13	106	This work

Supplementary Table 4 Comparison of the fractional free volume (FFV) of TB and QA-TB membranes with other membranes in the literature.

Type of membrane	Polymer structure	Fractional free volume (FFV)	Reference
PIM-Trip-TB	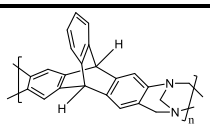	0.28	27
Bio-TBPI-2	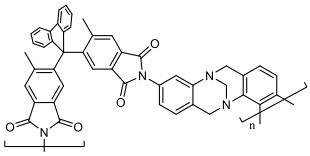	0.212	28
PI-TB-P	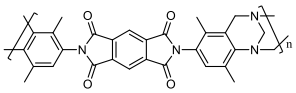	0.208	29
CA-PIM-2	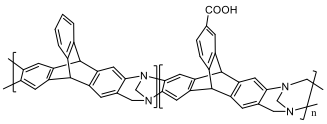	0.171	30
iPEEK-TB	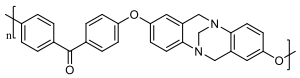	0.103	31
iPEEK-TB-p-DBX	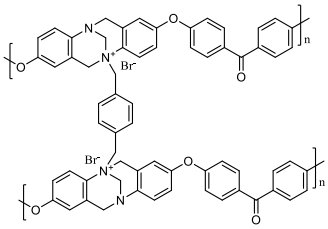	0.080	31
iPEEK-TB-o-DBX	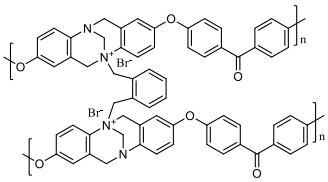	0.078	31
TB	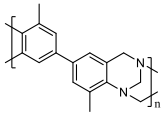	0.145	This work
QA-TB	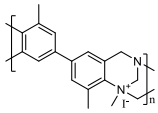	0.085	This work

Supplementary Table 5 Thermodynamic and physical characteristics of ions.

Ion	Diameter (nm)			Hydration free energy (KJ/mol)
	Crystal diameter (nm)	Stokes diameter (nm)[32, 33]	Hydrate diameter (nm)	
Cl^-	0.334[34] 0.362[35] 0.388[36]	0.242	0.648[37] 0.664[36]	-340[38] -355[34] -363[33] -371[39]
SO_4^{2-}	0.430[35] 0.460[34] 0.580[40]	0.460	0.758[33]	-1035[32] -1145[33]
CO_3^{2-}	0.144[32] 0.177[32]	0.532	0.788[32]	-1314[41] -1395[32]

Supplementary Table 6 Adsorption and desorption energies of different anions on the QA-TB.

QA-TB	Adsorption energy (eV)			Desorption energy (eV)
	Site 1	**Site 2**	**Site 3**	**Site 3**
Cl^-	-0.39	-0.48	-0.66	0.23
SO_4^{2-}	-0.63	-0.65	-0.88	0.41
CO_3^{2-}	-0.75	-0.87	-0.91	0.45

References

1. Dalwani M, Bargeman G, Hosseiny SS, Boerrigter M, Wessling M, Benes NE. Sulfonated poly(ether ether ketone) based composite membranes for nanofiltration of acidic and alkaline media. *J. Membr. Sci.* **381**, 81-89 (2011).
2. Lyons JL, Van de Walle CG. Computationally predicted energies and properties of defects in GaN. *npj Comput. Mater.* **3**, 12 (2017).
3. Lee M, Youn Y, Yim K, Han S. High-throughput ab initio calculations on dielectric constant and band gap of non-oxide dielectrics. *Sci. Rep.* **8**, 14794 (2018).
4. Emery AA, Wolverton C. High-throughput DFT calculations of formation energy, stability and oxygen vacancy formation energy of ABO3 perovskites. *Sci. Data.* **4**, 170153 (2017).
5. Henkelman G, Uberuaga BP, Jónsson H. A climbing image nudged elastic band method for finding saddle points and minimum energy paths. *J. Chem. Phys.* **113**, 9901-9904 (2000).
6. Selcuk S, Selloni A. DFT+U Study of the Surface Structure and Stability of Co3O4(110): Dependence on U. *J. Phys. Chem. C.* **119**, 9973-9979 (2015).
7. Dixit DK, Gandhi K, Dixit BK. Theoretical calculation of hydrogen desorption energies of calcium hydride clusters. *Int. J. Hydrog. Energy.* **37**, 3767-3771 (2012).
8. Chen JH, Choo YSL, Wang XH, Liu YJ, Yue XB, Gao XL, Gao WT, Zhang QG, Zhu AM, Liu QL. Effects of the crown ether cavity on the performance of anion exchange membranes. *J. Colloid Interface Sci.* **643**, 62-72 (2023).
9. Patnaik P, Hossain SM, Pal S, Sarkar S, Sharma R, Chatterjee U. Controlling the sub-nano ion channels by crosslinking in PVDF-based anion exchange membrane for enhanced mono/bivalent anion permselectivity and acid reclamation. *J. Membr. Sci.* **688**, 122105-122121 (2023).
10. Choudhury A, Patnaik P, Mondal R, Sarkar S, Chatterjee U. GO-anchored imidazolium based cross-linked composite anion exchange membranes for the enhancement in acid recovery via diffusion dialysis. *Chem. Eng. J.* **451**, 138901-138912 (2023).
11. Zhu C, Li J, Liao J, Chen Q, Xu Y, Ruan H, Shen J. Acid enrichment via electrodialyser fabricated with poly(vinyl chloride)-based anion exchange membrane: Effect of hydrophobicity of aliphatic side-chains tethered on imidazolium groups. *Sep. Purif. Technol.* **293**, 120907-120919 (2022).
12. Chen Q, Yao Y, Liao J, Li J, Xu J, Wang T, Tang Y, Xu Y, Ruan H, Shen J. Subnanometer Ion Channel Anion Exchange Membranes Having a Rigid Benzimidazole Structure for Selective Anion Separation. *ACS Nano* **16**, 4629-4641 (2022).
13. Ju M, Ren Q, Xu J, Chen X, Meng L, Lei J, Zhao P, Wang Z. Construction of alkali-stable anion exchange membranes with hydrophilic/hydrophobic microphase separation structure by adjusting side chain length. *Chem. Eng. J.* **466**, 143023-143035 (2023).

14. Chen JH, Yue XB, Choo YSL, Yu Z, Wang XH, Gao XL, Gao WT, Zhang QG, Zhu AM, Liu QL. Tailoring the microphase separation structure of poly(crown ether) anion exchange membranes by introducing aliphatic chains. *J. Power Sources.* **570**, 233014-233023 (2023).
15. Zhang X, Cao Y, Zhang M, Wang Y, Tang H, Li N. Olefin metathesis-crosslinked, bulky imidazolium-based anion exchange membranes with excellent base stability and mechanical properties. *J. Membr. Sci.* **598**, 117793-117804 (2020).
16. Li J, Xu Z, Liao J, Ang EH, Chen X, Mu J, Shen J. Revolutionary MOF-enhanced anion exchange membrane for precise monovalent anion separation through structural optimization and doping. *Desalination* **576**, 117352-117366 (2024).
17. Yang J, Chen Q, Afsar NU, Ge L, Xu T. Poly(alkyl-biphenyl pyridinium)-Based Anion Exchange Membranes with Alkyl Side Chains Enable High Anion Permselectivity and Monovalent Ion Flux. *Membranes* **13**, 188-200 (2023).
18. Xu T, Wang Y, Chen Q, Zhu Y, Li W, Sheng F, Ge L, Li X, Xu T. Scalable and interfacial gap-free mixed matrix membranes for efficient anion separation. *AIChE J.* **70**, 18242-18252 (2023).
19. Irfan M, Ge L, Wang Y, Yang Z, Xu T. Hydrophobic Side Chains Impart Anion Exchange Membranes with High Monovalent–Divalent Anion Selectivity in Electrodialysis. *Chem. Eng.* **7**, 4429-4442 (2019).
20. Li J, Qian H, Liao J, Li Y, Xu J, Chen Q, Yao Y, Mu J, Xu Y, Ruan H, Xu X, Shen J. Enhanced monovalent anion selectivity of poly(2,6-dimethyl-1,4-phenylene oxide)-based amphoteric ion exchange membranes having rough surface. *J. Membr. Sci.* **661**, 120911-120926 (2022).
21. Wang Y, Ren L, Wang J, Zhao J, Chen Q-B. In-situ growth of anionic covalent organic frameworks efficaciously enhanced the monovalent selectivity of anion exchange membranes. *J. Membr. Sci.* **659**, 120818-120827 (2022).
22. Liao J, Chen Q, Pan N, Yu X, Gao X, Shen J, Gao C. Amphoteric blend ion-exchange membranes for separating monovalent and bivalent anions in electrodialysis. *Sep. Purif. Technol.* **242**, 116793-116806 (2020).
23. Liao J, Yu X, Pan N, Li J, Shen J, Gao C. Amphoteric ion-exchange membranes with superior mono-/bi-valent anion separation performance for electrodialysis applications. *J. Membr. Sci.* **577**, 153-164 (2019).
24. Mondal R, Sarkar S, Patnaik P, Chatterjee U. Preparation of a Monovalent-Selective Anion-Exchange Membrane: Effect of Alkyl Chain Length and Crystallinity. *ACS Appl. Polym.* **5**, 2513-2524 (2023).
25. Gangrade AS, Tusi B, Ghosh PC, Holdcroft S. High monovalent/divalent permselectivity and low ionic resistance of ionene-based anion exchange membranes in electrodialysis. *J. Membr. Sci.* **685**, 121906-121919 (2023).
26. Zhang H, Ding R, Zhang Y, Shi B, Wang J, Liu J. Stably coating loose and electronegative thin layer on anion exchange membrane for efficient and selective monovalent anion transfer. *Desalination* **410**, 55-65 (2017).
27. Balcik M, Wang Y, Pinnau I. Exploring the effect of intra-chain rigidity on

mixed-gas separation performance of a Triptycene-Tröger's base ladder polymer (PIM-Trip-TB) by atomistic simulations. *J. Membr. Sci.* **677**, 121614-121622 (2023).

28. Hu X, Lee WH, Zhao J, Bae JY, Kim JS, Wang Z, Yan J, Zhuang Y, Lee YM. Tröger's Base (TB)-containing polyimide membranes derived from bio-based dianhydrides for gas separations. *J. Membr. Sci.* **610**, 118255-118265 (2020).
29. Lu J, Zhang Y, Li J, Fu M, Zou G, Ando S, Zhuang Y. Tröger's Base (TB)-Based Polyimides as Promising Heat-Insulating and Low-K Dielectric Materials. *Macromolecules* **56**, 2164-2174 (2023).
30. Zhang T, Deng L, Li P. Decarboxylation Cross-Linking of Triptycene-Based Tröger's Base Polymers for Gas Separation. *Ind. Eng. Chem. Res.* **59**, 18640-18648 (2020).
31. Abdulhamid MA, Hardian R, Szekely G. Waltzing around the stereochemistry of membrane crosslinkers for precise molecular sieving in organic solvents. *J. Membr. Sci.* **638**, 119724-119734 (2021).
32. Zhao Y, Mamrol N, Tarpeh WA, Yang X, Gao C, Van der Bruggen B. Advanced ion transfer materials in electro-driven membrane processes for sustainable ion-resource extraction and recovery. *Prog. Mater. Sci.* **128**, 100958-100988 (2022).
33. E.R. Nightingale, Phenomenological theory of ion salvation-effective radii of hydrated ions, *J. Phys. Chem.* **63**, 1381-1387 (1959).
34. Tansel B. Significance of thermodynamic and physical characteristics on permeation of ions during membrane separation: Hydrated radius, hydration free energy and viscous effects. *Sep. Purif. Technol.* **86**, 119-126 (2012).
35. M.Y. Kiriukhin, K.D. Collins, Dynamic hydration numbers for biologically important ions, Biophys. *Chem.* **99**, 155-168 (2002).
36. A.G. Volkov, S. Paula, D.W. Deamer, Two mechanisms of permeation of small neutral molecules and hydrates ions across phospholipid bilayers, Bioelectrochem. *Bioenerget.* **42**, 153-160 (1997).
37. J. Zhou, X. Lu, Y. Wang, J. Shi, Molecular dynamics study on ionic hydration, *Fluid Phase Equilibria* **194-197**, 257-270 (2002).
38. H. Binder, O. Zschornig, The effect of metal cations on the phase behavior and hydration characteristics of phospholipid membranes, *Chem. Phys. Lipids.* **115**, 39-61 (2002).
39. G. Hummer, L.R. Pratt, A.E. Garcia, Free Energy of Ionic Hydration, *J. Phys. Chem.* **100**, 1206-1215 (1996).
40. Collins K. Ions from the Hofmeister series and osmolytes: effects on proteins in solution and in the crystallization process. *Methods* **34**, 300-311 (2004).
41. Smith DW. Ionic Hydration Enthalpies. *J. Chem. Educ.* **54**, 540-542 (1977).